Isopycnal eddy stirring dominates thermohaline mixing in the upper subpolar North Atlantic

Bieito Fernández Castro[1], Daniel Fernandez Roman[2], Bruno Ferron[3], Marcos Fontela[4], Pascale Lherminier[5], Alberto C. Naveira Garabato[1], Fiz Pérez[6], Carl Pranas Spingys[7], Kurt Polzin[8], and Anton Velo[6]

[1]University of Southampton
[2]Universidade de Vigo
[3]French National Centre for Scientific Research (CNRS)
[4]Instituto de Investigacións Mariñas, IIM-CSIC
[5]Ifremer
[6]Instituto de Investigaciones Marinas. IIM-CSIC
[7]National Oceanography Centre
[8]Woods Hole Oceanographic Institution

May 28, 2024

Isopycnal eddy stirring dominates thermohaline mixing in the upper subpolar North Atlantic

Bieito Fernández Castro[1], Daniel Fernández Román[2], Bruno Ferron[3], Marcos Fontela[4], Pascale Lherminier[3], Alberto Naveira Garabato[1], Fiz F. Pérez[4], Carl Spingys[5], Kurt Polzin[6], and Antón Velo[4]

[1]Ocean and Earth Science, National Oceanography Centre, University of Southampton, Southampton, UK
[2]Centro de Investigacións Mariñas, Universidade de Vigo (CIM-UVigo), Vigo, Spain
[3]University of Brest, CNRS, Ifremer, IRD, Laboratoire d'Océanographie Physique et Spatiale (LOPS), IUEM, F29280, Plouzané, France
[4]Instituto de Investigacións Mariñas, IIM-CSIC, Vigo, Spain
[5]National Oceanography Centre, Southampton, UK
[6]Woods Hole Oceanographic Institution, Woods Hole, USA

Key Points:

- We quantify diapycnal and isopycnal contributions to thermohaline mixing in the subpolar North Atlantic with microstructure observations
- Isopycnal stirring dominates thermohaline mixing, suggesting a key role in the water-mass transformations driving the overturning circulation
- The relative importance of isopycnal stirring is tracer-dependent, controlled by the large-scale co-variability of the tracer with density

Corresponding author: Bieito Fernández Castro, b.fernandez-castro@soton.ac.uk

Abstract

The Atlantic Meridional Overturning Circulation entails vigorous thermohaline transformations in the subpolar North Atlantic Ocean (SPNA). There, warm and saline waters originating in the (sub)tropics are converted into cooler and fresher waters by a combination of surface fluxes and sub-surface mixing. Using microstructure measurements and a small-scale variance conservation framework, we quantify the diapycnal and isopycnal contributions –by microscale turbulence and mesoscale eddies, respectively– to thermohaline mixing within the eastern SPNA. Isopycnal stirring is found to account for the majority of thermal (65%) and haline (84%) variance dissipation in the upper 400 m of the eastern SPNA. A simple dimensional analysis suggests that isopycnal stirring could account for $\mathcal{O}$(5-10) Sv of diahaline volume flux, suggesting an important role of such stirring in regional water-mass transformations. Our mixing measurements are thus consistent with recent indirect estimates in highlighting the importance of isopycnal stirring for North Atlantic overturning.

Plain Language Summary

The North Atlantic hosts an ocean circulation system called the Atlantic Meridional Overturning Circulation (AMOC). It is often likened to a giant conveyor belt in the ocean, moving warm, salty waters from south to north and transforming them into cold, fresh waters that flow back southward at greater depth. The AMOC is a crucial element of the Earth's climate, and if it were to slow down, it could lead to major climatic changes. For a long time, scientists thought that the AMOC was mainly driven by cooling in the North Atlantic. But recently, we have discovered that the mixing of different water masses is also important. In our study, we used small-scale measurements of ocean properties to examine the processes behind this mixing. Our findings show that large swirling flows known as mesoscale eddies, which are tens to hundreds of kilometers wide and hundreds of meters deep, play a dominant role in mixing heat and salt in the North Atlantic. This discovery helps us to better understand the AMOC and its future behavior.

1 Introduction

The subpolar North Atlantic (SPNA) is a hotspot of ocean ventilation, resulting in significant exchanges of heat and greenhouse gases with the atmosphere (Pérez et al., 2013). This makes the SPNA an important region in the regulation of Earth's climate. The relevance of the SPNA for ocean ventilation and climate is rooted in its central role in the global meridional overturning circulation (MOC) (Daniault et al., 2016; Lozier et al., 2019). Within the cyclonic pathways of the SPNA gyre, vigorous water mass transformations convert warm and salty central waters into cooler, fresher and denser subpolar mode waters (SPMW) (McCartney & Talley, 1982; Brambilla & Talley, 2008; García-Ibáñez et al., 2015; Berglund et al., 2023) and intermediate waters. These intermediate waters are formed through deep convection in the Irminger (Pickart et al., 2003; De Jong et al., 2012) and Labrador Seas (Lazier et al., 2002). Together with denser overflows from the Nordic Seas, SPNA-produced waters constitute the lower limb of the Atlantic MOC (AMOC), which flows southward within a Deep Western Boundary Current along the North American margin (Daniault et al., 2016; Lozier et al., 2019).

Traditionally, deep convection in the Labrador Sea was considered the primary source of dense water for the AMOC. However, recent observations and modelling studies have led to a paradigm shift, by which the majority of the light-to-dense water mass conversion driving the AMOC is recognized to occur in the eastern SPNA (eSPNA), specifically in the Irminger and Nordic Seas (Lozier et al., 2019; Petit et al., 2020; Yeager et al., 2021). Further, while conventional understanding portrays the AMOC as an intrinsically diapycnal process, recent investigations suggest that water-mass transformations in the SPNA involve large density-compensated (isopycnal) temperature and salinity changes (Zou et al., 2020; Evans et al., 2023).

Finally, closure of the AMOC in the SPNA has been traditionally attributed to atmospheric cooling (Marsh, 2000; Petit et al., 2020), yet there is growing evidence that interior thermohaline transformations, driven by mixing along and across density surfaces, are necessary for sustaining the AMOC (Xu et al., 2018; Brüggemann & Katsman, 2019; Mackay et al., 2020; Evans et al., 2023; Tooth et al., 2023; Bebieva & Lozier, 2023; Berglund et al., 2023). Diapycnal mixing contributes, for example, to the densification of SPMW through entrainment of overflow waters (Evans et al., 2023). In turn, mixing associated with isopycnal eddy stirring delivers salt into the subpolar gyre, enabling an increase in the density of lower-limb waters (Warren, 1983; Pradal & Gnanadesikan, 2014; Born et al., 2016; Evans et al., 2023). Finally, mesoscale eddies transfer, via advection and mixing, intermediate waters produced by deep convection in the Labrador and Irminger basins into the Deep Western Boundary Current, thereby connecting such waters to the AMOC (Straneo, 2006; Brüggemann & Katsman, 2019; Mackay et al., 2020).

Despite the increasingly acknowledged importance of interior thermohaline transformations in the SPNA, direct observations in the area are scarce (Lauderdale et al., 2008; Jurado, van der Woerd, & Dijkstra, 2012; Jurado, Dijkstra, & van der Woerd, 2012; Ferron et al., 2014; Kunze et al., 2023), and quantification relies largely on indirect mixing estimates via inverse methods and model output analyses (Xu et al., 2018; Mackay et al., 2020; Evans et al., 2023; Tooth et al., 2023). Consequently, the nature of the processes driving these transformations remains largely unknown.

Mixing – the destruction of property contrasts by molecular diffusion– results from a downscale variance cascade driven by the stirring of isopycnal property gradients by mesoscale eddies (horizontal scale > 10 km), and the mixing of diapycnal property gradients by microscale turbulence (horizontal and vertical scales < 10 m) (Lee et al., 1997; Garrett, 2001; Ferrari & Polzin, 2005; Naveira Garabato et al., 2016). The small- and mesoscale regimes are underpinned by different dynamics, and are likely to exhibit distinct sensitivities to changes in forcing and potential feedbacks on the AMOC. A deeper

understanding of SPNA mixing processes is thus essential for unravelling the AMOC's dynamics and long-term evolution.

Pioneering work in the Southern Ocean demonstrates that microstructure turbulence observations can be used to elucidate the links between mixing, thermohaline transformations and overturning circulation, and to identify the processes responsible for such mixing (Naveira Garabato et al., 2016; Orúe-Echevarría et al., 2023). In this study, we address the role of mixing in SPNA thermohaline transformations by analyzing a set of microstructure temperature and shear profiles, collected across the eSPNA, within a tracer variance budget framework (Ferrari & Polzin, 2005; Naveira Garabato et al., 2016), allowing us to disentangle the diapycnal and isopycnal contributions to mixing. Our analysis reveals that isopycnal stirring dominates thermal and, more distinctly, haline mixing in the upper layers of the eSPNA, indicating and important contribution of mesoscale turbulence to the water-mass transformations responsible for the AMOC's closure in the SPNA.

2 Methods

2.1 Observations

Microstructure data were collected during the BOCATS2 2023 cruise across the North Atlantic Ocean from 9th June to 11th July 2023. The mission sampled the OVIDE repeated hydrography section (WOCE A25) between Portugal and Cape Farewell (Greenland) (Lherminier et al., 2010, 2023), and two additional sections across the East Greenland Current (EGC) and the Irminger Sea, north of the A25-OVIDE line (Fig.1a). Microstructure turbulence profiles were collected in 32 stations with a microstructure profiler (MSS, Prandke and Stips (1998)). A total of 94 profiles were obtained, with 1-3 profiles per station, except in the last station (station 32) over the Reykjanes Ridge at 61.14°N, 27.97°. There, a time-series consisting of 21 profiles was recorded during a 14-hour period (TS label in Fig.1). Profiles were performed down to depths of 300-400 m, except in shallower stations of the EGC.

The MSS is equipped with two shear microstructure sensors and a temperature microstructure sensor, complemented with a Sea&Sun high-accuracy Conductivity-Temperature-Depth (CTD) suite. The instrument is loosely-tethered and operates in free-falling mode at a vertical speed of 0.6–0.7 m s^{-1}, sampling all variables at 1024 Hz. Profiles of conservative temperature (Θ), practical salinity (S_A) and surface-referenced potential density (σ_0) with 1 m vertical resolution were derived by bin-averaging the CTD output. The dissipation rates of turbulent kinetic energy (ε) and thermal variance (χ_Θ) were computed from the microstructure shear and temperature measurements, respectively, with a vertical resolution of 1 m from overlapping data segments of 4 m length following Piccolroaz et al. (2021) and Fernández Castro et al. (2022).

Generally, ε and χ_Θ were determined by integration of the shear and temperature gradient spectra over the well-resolved wavenumber ranges, and the variance outside those ranges was recovered using empirical spectral forms (Nasmyth and Kraichnan, respectively) (Fernández Castro et al., 2022). Pairs of measured shear and temperature, randomly selected over the range of representative values, are presented in Fig. 2, showing a good agreement with the corresponding empirical spectra. Due to weak turbulence, shear-based ε estimates occasionally approached the instrument's noise floor of $\mathcal{O}(10^{-9}\,\mathrm{W\,kg^{-1}})$. In those instances, ε was derived through fitting the temperature gradient spectrum to the Kraichnan spectrum (Piccolroaz et al., 2021), as this technique has a lower noise floor of $\mathcal{O}(10^{-12}\,\mathrm{W\,kg^{-1}})$. For consistency, in those instances χ_Θ was also derived from spectral fits.

2.2 Triple decomposition of the tracer variance budget: theory

To investigate the relative contribution of small- and mesoscale turbulence to thermohaline mixing, we followed a triple decomposition of the small-scale tracer variance conservation equation (Joyce, 1977; Davis, 1994; Garrett, 2001; Ferrari & Polzin, 2005). This decomposition is founded on the interpretation of mixing as a tracer variance transfer from the basin scale (where variance is introduced, e.g., by air-sea fluxes) to centimeter scales, where it is dissipated by molecular processes. The variance cascade follows two main pathways, mediated by mesoscale and microscale turbulence, respectively, as summarized in a diagram proposed by Garrett (2001):

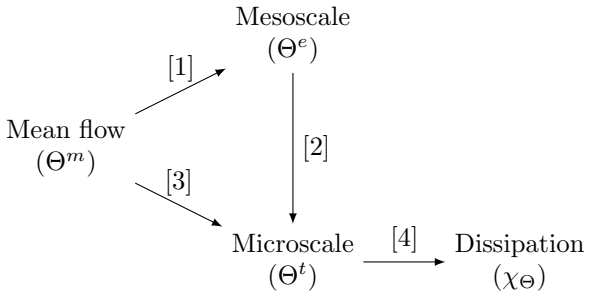

(1)

Here, we used conservative temperature (Θ) as our reference tracer, and decomposed the spatio-temporal distribution of Θ into the sum of three terms, $\Theta = \Theta^m + \Theta^e + \Theta^t$. Θ^m represents the large-scale, slowly-varying (typically >100 km in the horizontal, >100 m in the vertical, months to years and over, in time) mean distribution of temperature; Θ^e represents mesoscale (10-100 km in the horizontal, 10-100 m in the vertical, days to months in time) fluctuations; Θ^t are the microscale (<10 m in space, seconds to hours in time) fluctuations associated with isotropic turbulence; and χ_Θ is the rate of thermal variance dissipation by molecular processes.

In the microscale pathway ([3] $\rightarrow$ [4]), microscale isotropic turbulence transfers tracer variance from the mean flow directly into microscale variability (Θ^t) and dissipation. This transfer is mediated by microscale overturns of the mean vertical density profile, i.e. through stirring of the diapycnal tracer gradient. The mesoscale route ([1] $\rightarrow$ [2] $\rightarrow$ [4]) starts with the stirring of tracer gradients along isopycnal surfaces, which results in the creation of vertical fine-scale structures in the range of 10-100 m (Fig. 3). The variance stored in such mesoscale fluctuations (Θ^e) is finally transferred to dissipation scales by microscale overturning turbulence.

Traditionally, microstructure studies have focused on the variance transfer to the microscale and dissipation (the combined effect of [2] + [3], leading to [4]) and expressed the tracer variance conservation equation in a two-term Reynolds decomposition framework. In this framework, the flow components are separated into the sum of turbulent fluctuations (<10 m) and a mean flow component ($\Theta = \overline{\Theta} + \Theta^t$), which includes both the large-scale mean flow and mesoscale fluctuations ($\overline{\Theta} = \Theta^m + \Theta^e$). In practice, in oceanographic studies, turbulent fluctuations (Θ^t) are defined as those related to microscale three-dimensional turbulence (<10 m), which results in diapycnal tracer mixing, and can only be measured with microstructure instruments. The mean flow component ($\overline{\Theta}$) covers multi-meter scales of variability, which are resolved by standard (CTD) oceanographic measurements. The latter $\overline{\Theta}$ includes the basin-scale tracer contrasts, but also fine-scale structures due to stirring by mesoscale motions along isopycnal surfaces (Ferrari & Polzin, 2005).

In the two-term Reynolds framework, and in the limit of flow and tracer fluctuations being statistically stationary and homogeneous, the tracer variance conservation

is expressed as:

$$\underbrace{-2\overline{\mathbf{u}^t\Theta^t}\cdot\nabla\overline{\Theta}}_{P_{\Theta^2}} = \underbrace{2\kappa_\Theta\overline{(\nabla\Theta^t)^2}}_{\chi_\Theta} \tag{2}$$

where $\mathbf{u}$ is the flow velocity, ∇ is a three-dimensional gradient operator, and κ_Θ is the molecular diffusivity of heat. This equation expresses a local balance between the production of small-scale tracer variance, P_{Θ^2}, due to the stirring of the mean-flow three-dimensional tracer gradient ($\nabla\overline{\Theta}$) by turbulent eddies (which results from the combined downscale transfer via the mesoscale and microscale routes, [1]+[3]), and its dissipation by molecular diffusion, χ_Θ or [4].

By taking a gradient flux approximation ($\overline{\mathbf{u}^t\Theta^t} = -K_\rho\nabla\overline{\Theta}$), and using the facts that diapycnal gradients are much larger than isopycnal gradients and isopycnal layers are close to horizontal ($|\nabla\overline{\Theta}| \approx |\partial\overline{\Theta}/\partial z|$), tracer variance dissipation can be related to a microscale turbulent diapycnal diffusivity (K_ρ) via the widely-used Osborn and Cox (1972) formula:

$$\chi_\Theta = P_{\Theta^2} \approx 2K_\rho\left(\frac{\partial\overline{\Theta}}{\partial z}\right)^2 \tag{3}$$

The triple variance decomposition allows one to separately account for the contributions of mesoscale (isopycnal) stirring and microscale turbulence (diapycnal mixing) to the variance cascade. In this framework, the tracer variance conservation equation is expressed as (Ferrari & Polzin, 2005):

$$\underbrace{-2\langle\mathbf{u}^t\Theta^t\rangle\cdot\nabla_\perp\Theta^m}_{P^\perp_{\Theta^2}}\underbrace{-2\langle\mathbf{u}^e\Theta^e\rangle\cdot\nabla_{||}\Theta^m}_{P^{||}_{\Theta^2}} = \chi_\Theta, \tag{4}$$

where angled brackets represent an average over large spatial scales in comparison with mesoscale fluctuations, but small in comparison with the large-scale mean flow; and $\nabla_\perp$ and $\nabla_{||}$ respectively denote gradient operators across and along density surfaces. In this framework, the dissipation of thermal variance [4] is thus balanced by the stirring of the mean diapycnal gradient by microscale turbulence ($P^\perp_{\Theta^2}$ or [3]) plus the stirring of the large-scale isopycnal gradients by mesoscale motions ($P^{||}_{\Theta^2}$, [1]). Mesoscale stirring generates fine-scale vertical (10-100 m) structures, whose variance is then transferred to the microscale by microscale turbulence ([2]), eventually resulting in molecular dissipation ([4]).

By applying a flux-gradient relationship, $P^\perp_{\Theta^2}$ can be linked to the microscale diapycnal diffusivity:

$$P^\perp_{\Theta^2} = 2K_\rho(\nabla_\perp\Theta^m)^2, \tag{5}$$

and the contribution of eddy stirring to mixing can be diagnosed as:

$$P^{||}_{\Theta^2} = \chi_\Theta - P^\perp_{\Theta^2} = \chi_\Theta - 2K_\rho(\nabla_\perp\Theta^m)^2. \tag{6}$$

2.3 Triple decomposition of the tracer variance budget: Implementation

By applying the variance budget framework (Eqs. 4-6) to BOCATS2 microstructure data, we assessed the relative contribution of microscale turbulence and mesoscale stirring to the mixing of heat (and salt) in the eSPNA. To do so, we used microstructure observations of χ_Θ to quantify total heat mixing, and we estimated the contribution of microscale turbulence by quantifying $P^\perp_{\Theta^2}$ using equation 5. We finally inferred the contribution of isopycnal stirring from the difference between χ_Θ and $P^\perp_{\Theta^2}$ (Eq. 6).

Quantifying the contribution of microscale turbulence to mixing (i.e. diapycnal mixing) from observed $\overline{\Theta}$ profiles (here the overbar denotes tracer profiles measured by our

profiler's CTD probe with meter-scale resolution) involves some degree of spatial or temporal averaging to remove fluctuations associated with mesoscale stirring, to estimate Θ^m and compute $P^{\perp}_{\Theta^2}$ via Eq. 5 (Ferrari & Polzin, 2005). Such averaging is impractical in most stations of our dataset, where spatio-temporal information is lacking. To overcome this limitation, we smoothed the measured profiles through a 4-degree polynomial fit against σ_0 over the full range of measured depths, in order to obtain a set of Θ^m profiles (see example in Fig. 3):

$$\Theta^m = f(a_0 + a_1 \cdot \sigma_0 + \ldots + a_4 \cdot \sigma_0^4) \tag{7}$$

Although the choice of a 4-degree polynomial is somewhat arbitrary, our results proved relatively insensitive to the precise choice or smoothing method.

This approach removes the density-compensated vertical fine-scale structures (10−100 m length scales) associated with isopycnal stirring. Those structures are the element connecting the mesoscale variance cascade to microscale turbulence and dissipation. Therefore, removing the fine-scale vertical structures allows one to isolate the contribution of mesoscale stirring from the observed mixing. Herewith, we refer to this particular form of Θ^m profiles as "background" profiles, instead of the more general "large-scale mean" profiles, to avoid the ambiguity of scale in the definition of a "large-scale mean".

The diapycnal production term (Eq. 5) was then estimated using the vertical gradients of Θ^m, assuming that isopycnals are nearly horizontal:

$$P^{\perp}_{\Theta^2} = 2K_\rho \left(\frac{\partial \Theta^m}{\partial z} \right)^2 . \tag{8}$$

Here, the diapycnal diffusivity was calculated using the Osborn (1980) formula:

$$K_\rho = \Gamma \frac{\varepsilon}{\overline{N}^2} \tag{9}$$

where Γ is the mixing efficiency, assumed to take a constant value of $\Gamma = 0.2$ (Oakey, 1982), and $\overline{N}^2 = -g/\rho \partial \bar{\rho}/\partial z$ is the buoyancy frequency. The density gradient is calculated by linear fitting of the measured density profile against depth over 4 m segments (the same vertical scale over which ε and χ_Θ are calculated).

The same diagnosis of the mixing contributions was performed for salinity. However, while $P^{\perp}_{S^2}$ is computed in the same way as $P^{\perp}_{\Theta^2}$, χ_S could not be obtained directly from microstructure salinity observations as those were not available. We circumvented this issue by using the Osborn and Cox (1972) formula (Eq. 3) to estimate χ_S from K_ρ and the fine-scale vertical salinity gradient as measured by the microprofiler's CTD suite ($\partial \overline{S}_A/\partial z$):

$$\chi_S \approx 2K_\rho \left(\frac{\partial \overline{S}_A}{\partial z} \right)^2 , \tag{10}$$

where $\partial \overline{S}_A/\partial z$ is determined by linear fitting over 4 m segments (similar to $\overline{N}^2$). This approximation assumes that χ_S is balanced locally by the effect of stirring by microscale turbulence on fine-scale tracer gradients (P_{S^2}). The assumption is clearly met for Θ, for which χ_Θ and P_{Θ^2} agree within a factor of 2 over 5 orders of magnitude (Fig. 4), suggesting that Eq. 10 is an adequate approximation for estimating χ_S.

3 Results

3.1 Hygrography

The BOCATS2 microstructure survey stations covered the broad range of hydrographic conditions characterising the eSPNA, which reflect the transformation of central waters into SPMW (McCartney & Talley, 1982; Brambilla & Talley, 2008; García-Ibáñez et al., 2015; Stendardo et al., 2024). The eastern section (stations 1-10, Fig 1)

sampled the relatively warm (10-20 °C), salty (> 35.75 g kg^{-1}) and light (σ_0 < 27.4 kg m^{-3}) central waters of the Western European Basin (WEB) (Fig. 5). The upper ocean (<400 m) of the WEB was strongly stratified, with a ∼1 kg m^{-3} contrast between the upper and deeper sampled layers (Fig. 5c, 6a). WEB stratification was dominated by temperature differences, whilst haline stratification was weakly unstable (Fig. 5a,b, 6a). The western sections sampled across the Irminger Sea (IrmS) and the East Greenland Current (EGC) (Fig. 1). Below a shallow seasonal thermocline, IrmS waters were cooler (3-11 °C) and fresher (35.0-35.6 g kg^{-1}) than WEB waters, and also denser, with σ_0 > 27.5 kg m^{-3} (Fig. 5), as is characteristic of SPMW (Brambilla & Talley, 2008; Stendardo et al., 2024). The upper IrmS was also thermally stratified, but more weakly than the WEB, with a density difference of ∼0.7 kg m^{-3} (Fig. 6a). The salinity profiles were rather homogeneous (Fig. 5b), resulting in very weak haline stratification (Fig. 6a). Finally, the offshore waters of the EGC showed a large overlap in thermohaline properties with IrmS waters, at least below 100 m depth. However, shallower depths were markedly cooler, fresher and lighter, particularly in the inner EGC, with temperatures and salinities as low as -1°C and 30 g kg^{-1} (Fig. 5). Contrary to the WEB and IrmS, the strong stratification of EGC waters (>1 kg m^{-3} in inshore stations) was salinity-driven (Fig. 6a).

Overall, BOCATS2 sampled across a northwestward gradient of decreasing temperature and salinity, which is partially density-compensated. This partial compensation permits the existence of substantial thermohaline gradients along isopycnals (as seen in the climatological S_A distribution shown in Fig. 1a). Mesoscale eddies acting on these large-scale thermohaline gradients produce measurable density-compensated thermohaline fine-scale vertical structures (Fig. 5a,b). Such fine structures make different contributions to the overall vertical variance of Θ and S_A in different regions (Fig. 6b), reflecting the relative importance of isopycnal stirring. Due to the strong thermal stratification in the WEB and IrmS, almost 100% of the Θ vertical variance corresponds to the background profile (Θ^m), although density-compensated fine-scale thermal structures associated with eddy stirring were also evident there (Fig. 5a). Fine-scale structures had a larger imprint on salinity vertical variance in those same regions, where the background salinity profile (S_A^m) contained only 50-80% of the S_A variance, due to the weak salinity stratification (Fig. 6b). The reverse scenario was encountered in the salinity-stratified EGC region, where most of S_A variance was explained by S_A^m, and Θ fine structures made a variable but larger (up to 50%) contribution to thermal variance.

3.2 Isopycnal stirring and diapycnal mixing from a time-series station

The occurrence of density-compensated thermohaline fine structures, and their temporal variability, is clearly illustrated in the 14-hour time-series station data at the Reykjanes Ridge (Fig. 7). As the rest of the IrmS, the sampling site was thermally-stratified with a thermocline at around 50 m depth (Fig. 7a), while salinity did not exhibit a well-defined mean vertical structure (Fig. 7b). Instead, there was substantial temporal and vertical fine-scale variability (Fig. 7b,d). Although some isopycnal heaving was apparent, thermohaline variability occurred mostly at constant density, as salinity anomalies were mirrored by opposing temperature anomalies (Fig. 7c,d). The site was rather turbulent, with ε and χ_Θ values of $10^{-8} - 10^{-7}$ W kg^{-1} and $10^{-7} - 10^{-6}$ K^2 s^{-1} in the surface layer and thermocline, and recurrent patches of comparably intense turbulence and mixing in deeper layers (Fig. 7a,b).

The mean rates of thermal variance dissipation (χ_Θ – from microstructure measurements) and diapycnal production ($P^{\perp}_{\Theta^2}$, Eq. 5), were similar at 10^{-7} K^2 s^{-1} in the shallow thermocline (Fig. 8a), indicating a dominance of thermal mixing by microscale turbulence. However, below 100 m depth, χ_Θ was consistently higher than $P^{\perp}_{\Theta^2}$, due to the intensification of thermal mixing associated with fine-scale eddy-induced variability. When averaged below 100 m, $P^{\perp}_{\Theta^2}$ (0.16×10^{-8} K^2 s^{-1}) accounted for about one third of the overall χ_Θ (0.49×10^{-8} K^2 s^{-1}) (Fig. 8a). Therefore, eddy stirring was the

main driver of thermal mixing below the seasonal thermocline. Due to the lack of a well-defined mean diapycnal salinity gradient, the contribution of eddy stirring to salinity mixing was overwhelmingly dominant, even within the thermocline (Fig. 8b), as diapycnal production ($P^{\perp}_{S^2} = 0.17{\times}10^{-11}$ (g kg^{-1})^2 s^{-1}) explained only 1.3% of the haline variance dissipation ($\chi_S = 1.27 \times 10^{-10}$ (g kg^{-1})^2 s^{-1}).

3.3 Regional patterns in isopycnal stirring and diapycnal mixing

The analysis of all the microstructure profiles recorded during BOCATS2 was consistent with the overall dominance of mesoscale stirring below the seasonal pycnocline (∼100 m), for both temperature and salinity mixing (Figs. 9a, 10a). On average, microscale turbulence accounted for 37% of the observed mean χ_Θ ($1.82{\times}10^{-8}$ K^2 s^{-1}), and for 17% of the mean χ_S (6.4×10^{-10} (g kg^{-1})^2 s^{-1}). The cruise-mean values encapsulate substantial regional differences in both the intensity of mixing and the relative importance of diapycnal and isopycnal processes.

At the WEB, mixing below the seasonal thermocline was weaker than the cruise mean, at $\chi_\Theta = 0.39 \times 10^{-8}$ K^2 s^{-1} and $\chi_S = 2.9 \times 10^{-10}$ (g kg^{-1})^2 s^{-1} (Figs. 9b, 10b). In this thermally stratified basin, diapycnal production was sufficient to explain almost all (84%) of the observed thermal mixing (Fig. 9b), while its contribution to salinity mixing was close to the cruise-average value of 17% (Fig. 10b). The IrmS was characterised by intermediate variance destruction rates of $\chi_\Theta = 1.21 \times 10^{-8}$ K^2 s^{-1} and $\chi_S = 3.7 \times 10^{-10}$ (g kg^{-1})^2 s^{-1} and a dominant role of isopycnal stirring, as diapycnal production accounted for only 20% and 0.6% of the thermal and haline mixing, respectively (Fig. 9c, 10c). In the EGC region, where turbulent kinetic energy dissipation rates were large (Fig. 1b), the highest levels of mixing were observed at $\chi_\Theta = 8.07 \times 10^{-8}$ K^2 s^{-1} and $\chi_S = 27.0{\times}10^{-10}$ (g kg^{-1})^2 s^{-1} (Fig. 9d, 10d). In this salinity-stratified area, the relative contribution of diapycnal haline mixing was the highest of the cruise at 26%. The mean contribution of diapycnal mixing to thermal variance dissipation sat at intermediate values of 42% below the halocline. However, within the halocline, thermal mixing was largely associated with isopycnal stirring, consistent with the sharp fine-scale thermal structures observed there (Fig. 5a).

4 Limitations

4.1 Validity of assumptions

The triple decomposition framework employed in this study has great potential to unravel the contributions of microscale and mesoscale turbulence to mixing; however, the method relies on several assumptions and choices entailing uncertainties and potential biases. Here, we assess to which extent our main conclusions may be impacted by such uncertainties.

One key assumption is that the mixing efficiency is relatively constant at $\Gamma = 0.2$, which enables estimation of the diapycnal variance production ($P^{\perp}_{\Theta^2}$) via Eqs. 8 and 9. The validity of this assumption is strongly supported by the good agreement, throughout the cruise data set, between thermal variance dissipation (χ_Θ) and its production via turbulent stirring of fine-scale gradients (P_{Θ^2}) (Fig. 4), since the estimation of P_{Θ^2} involves the use of a constant $\Gamma = 0.2$ in Eq. 9. The relative constancy of the mixing efficiency is consistent with the dominant regime of turbulence in the region. An evaluation of the buoyancy Reynolds number ($Re_b = \varepsilon/(\nu\overline{N}^2)$, where $\nu \approx 10^{-6}$ m^2 s^{-1} is molecular viscosity) shows that ∼70% of our data below 50 m lay at intermediate Re_b values ($Re_b = 10 - 500$, Fig. 11), in a range in which mixing efficiency is expected to be almost constant at ∼0.2 (Ijichi et al., 2020).

The estimation of χ_S via the Osborn and Cox (1972) formula (Eq. 10), by equating it to P_{S^2}, involves the additional assumption that variance dissipation (χ_S) is balanced locally by production via turbulent stirring of fine-scale (1-10 m) gradients (P_{S^2}), in the context of the two-term Reynolds decomposition. Therefore, the temporal variability and advection terms in the small-scale variance conservation equation are neglected. A local balance between variance dissipation and production by microscale turbulence is also required for the computation of the diapycnal mixing rates ($P^{\perp}$) via Eq. 8 and, therefore, for our estimation of the relative contributions of microscale and mesoscale processes to mixing. The validity of this assumption is again strongly endorsed by the good agreement between χ_Θ and P_{Θ^2} (Fig. 4). To further ascertain the robustness the local production-dissipation balance and the approximation of χ_S by P_{S^2}, we repeated the temperature variance analysis presented in Fig. 9, using P_{Θ^2} instead of χ_Θ, and found good agreement (within a factor of 2 or less) with the original computations (Fig. 12).

A third relevant assumption is that double-diffusive processes make negligible contributions to the temperature and salinity variance budgets. The importance of double diffusion can also be ruled out on the grounds of the prevailing turbulence regime, as the observed intermediate levels of turbulence are likely to disrupt the development of double diffusive instabilities (St Laurent & Schmitt, 1999). Further, stratification conditions potentially conducive to double diffusion were only observed in the WEB, associated with unstable salinity stratification (Fig. 6a). However, the density ratio, $R_\rho = (\alpha\,\partial\overline{\Theta}/\partial z)/(\beta\,\partial\overline{S_A}/\partial z)$ was systematically greater than 2 there (not shown), indicating only weak salt fingering instability, which would be easily disrupted by shear-driven turbulence (St Laurent & Schmitt, 1999). This is also in line with the absence of well-defined thermohaline staircases, characteristic of double diffusion, throughout the BOCATS2 section (Fig. 5a,b).

In addition to these assumptions, the triple decomposition approach involves selecting a method for filtering density-compensated thermohaline fine structures from the measured property profiles to obtain the background Θ^{m}, S_A^{m} profiles, and diagnose the rate of downscale variance transfer by microscale turbulence ($P^{\perp}$). Due to the lack of data to obtain spatio-temporal averages, we chose to compute Θ^{m} and S_A^{m} through a polynomial fit to the observed $\overline{\Theta}$ and $\overline{S}_A$ against σ_0. This choice entails some degree of subjectivity and uncertainty. Furthermore, by construction of the approach, any misfit between the polynomial function and the actual $\overline{\Theta}$ and $\overline{S}_A$ tends to be density-compensated, resulting in potential overestimation of the contribution of isopcynal stirring to mixing.

To gauge how this uncertainty may influence our conclusions, we tested an alternative method using the time-series station dataset, for which we have enough data to estimate background profiles via time averaging. To obtain Θ^{m} and S_A^{m} for each vertical cast, we first calculated time-mean $\overline{\Theta}$ and $\overline{S}_A$ profiles as a function of σ_0 and then interpolated them onto the observed σ_0 from each cast. The vertical distribution and overall magnitude of the alternative $P^{\perp}$ profiles agree well with the original results, although depth-averaged $P^{\perp}_{\Theta^2}$ and $P^{\perp}_{S^2}$ are roughly 30% and 70% lower, respectively (Fig. 13, compared to Fig. 8). This would imply a larger contribution of isopycnal stirring than originally estimated. Thus, the potential overestimation of isopycnal stirring resulting from the function misfit is not relevant here. Instead, the apparent underestimation may arise from fitting a 4-degree polynomial to more slowly varying measured Θ and S_A profiles, yielding vertical gradients on the scale of $\lesssim$100 m, which may not be representative of the actual "large-scale mean" Θ^m, S_A^m distributions. At any rate, while there is some uncertainty associated with our calculations, the prevalence of isopycnal over diapycnal mixing emerges as a highly robust result.

4.2 Temporal variability

The main drawback of our observations and analysis is their limited spatio-temporal coverage, being restricted to the summer season of a specific year, whilst hydrographic

conditions vary across a broad range of timescales in the subpolar North Atlantic, from seasonal to decadal. Such changes may modulate the magnitude and significance of mixing and its drivers. Notably, over the past twenty years, the region has experienced a cycle of cooling and freshening culminating in 2016, and subsequent warming (Holliday et al., 2020; Desbruyères et al., 2021). To ascertain to which extent these changes may have led to different mixing conditions, we analyse a microstructure dataset collected in the WEB and IrmS during the OVIDE cruise 2008, prior to the onset of the freshening cycle (Fig. 14).

The mean thermal and haline variance dissipation and diapycnal production profiles (Fig. 14) are similar in magnitude and shape to 2023 observations (Figs. 9, 10). Depth-averaged χ_Θ were 0.75×10^{-8} K^2 s^{-1} and 0.72×10^{-8} K^2 s^{-1} in the WEB and IrmS, respectively, with diapycnal production accounting for 0.20×10^{-8} K^2 s^{-1} and 0.15×10^{-8} K^2 s^{-1} in each case (Fig. 14a,b). All rates are within a factor of two the 2023 observations (Fig. 9b,c). The relative contribution of diapycnal mixing was almost identical in the IrmS at 20%, but it was lower in the WEB at 27% compared to 84% in 2023. However, the χ_Θ and $P^{\perp}_{\Theta^2}$ profiles were generally closer in value in the WEB (Fig. 14a) than in the IrmS (Fig. 14b), as in 2023. Depth-averaged salinity variance dissipation rates were 3.2×10^{-10} (g kg^{-1})^2 s^{-1} and 4.9×10^{-10} (g kg^{-1})^2 s^{-1} (Fig. 14c,d), also very close to the 2023 values (Fig. 10b,c). The relative contributions of diapycnal mixing to haline variance dissipation were 12% and 2.7% in the WEB and IrmS, respectively, in line with similarly low contributions of 16% and 0.6% in 2023.

Overall, the analysis of the 2008 dataset suggests that our main findings hold on interannual time-scales. To gain insight into the role of seasonal variations, and further strengthen general confidence in our results, we estimated the contributions of microscale and mesoscale turbulence to mixing using an entirely independent approach based on annual-mean climatological data. We used long-term averaged temperature (and salinity) distributions from the World Ocean Atlas 2018 (Boyer et al., 2018), and global maps of diapycnal and isopycnal diffusivity from internal-wave (de Lavergne et al., 2020) and mixing-length theories (Groeskamp et al., 2020), to estimate diapycnal and isopycnal thermal (and haline) variance production rates. These terms were calculated as $P^{\perp}_{\Theta^2} = 2K_\rho(\nabla_\perp \Theta^m)^2$, and $P^{||}_{\Theta^2} = 2K_{||}(\nabla_{||}\Theta^m)^2$, respectively, where $K_{||}$ is the isopycnal diffusivity from Groeskamp et al. (2020) and K_ρ is the diapycnal diffusivity from de Lavergne et al. (2020). The diapycnal ($\nabla_\perp$) and isopycnal ($\nabla_{||}$) tracer gradients were estimated after mapping Θ (and S_A) onto neutral density coordinates. Following Eq. 4, we estimated thermal variance dissipation as $\chi_\Theta = P^{\perp}_{\Theta^2} + P^{||}_{\Theta^2}$, and equivalently for salinity. The different mixing rate profiles were interpolated from the climatology grid onto the locations of the BOCATS2 cruise stations.

Climatological mixing rates are included in Figs. 9b,c and 10b,c, with black dots showing total mixing (diapycnal plus isopycnal, that is, $\chi = P^{\perp} + P^{||}$) and blue dots showing diapycnal variance production ($P^{\perp}$). The climatological estimates compare well with observations, in terms of both the mixing rates' absolute values and the relative contributions of diapycnal and isopycnal processes (Fig. 9, 10). They are compatible with an important role of isopycnal stirring in the mixing of heat and, more substantially, salt in the IrmS (Fig. 9c, 10c); and a more notable contribution of diapycnal processes to thermal mixing in the WEB (Fig. 9b). Comparison in the EGC was not possible due to the lack of climatological data in this shallower region. The climatological estimates thus broadly align with our observational results, and lend some support to their relevance beyond the summer season of 2023.

5 Discussion

In our study, we leveraged a set of summertime microstructure observations in the eSPNA to assess the rates of variance dissipation by microscale diapycnal mixing and

mesoscale isopycnal stirring, respectively. While employing microstructure observations for investigating diapycnal mixing is a well-established technique in modern oceanography (Waterhouse et al., 2014), the quantification of isopycnal stirring using this approach remains relatively underexplored, with only a few notable exceptions (Ferrari & Polzin, 2005; Naveira Garabato et al., 2016; Orúe-Echevarría et al., 2023). Building upon this work, we base our analysis on a triple decomposition of the tracer variance conservation equation, along with measurements of ε and χ_Θ. Additionally, we extend previous efforts by applying the triple decomposition to the salinity variance budget, by using the Osborn and Cox (1972) equation to estimate χ_S.

Our analysis unveiled the dominance of mesoscale stirring in driving mixing of heat and, more importantly, salt across central water and SPMW layers of the upper eSPNA. These findings align with previous results derived from reanalysis and modeling datasets (Xu et al., 2018; Tooth et al., 2023), which emphasize the role of lateral mixing along the inter-gyre boundary and Polar Front in transforming central waters into SPMW, a key component of the AMOC (Evans et al., 2023; Berglund et al., 2023). Our measurements further indicate that the dominance of mesoscale processes is widespread, particularly in the Irminger Sea, extending beyond frontal regions. The highest rates of energy and variance dissipation were measured at the EGC, in line with previous observations (Lauderdale et al., 2008). Despite intense microscale turbulence there, isopycnal stirring was also the main driver of mixing at the EGC, accounting for >50% of heat and salt variance dissipation. This finding is consistent with vigorous isopycnal property exchanges between the ventilated basin interior and boundary currents, demonstrated in idealized and realistic simulations, as well as observations (Straneo, 2006; Brüggemann & Katsman, 2019; Mackay et al., 2020; Le Bras et al., 2020). Such exchange is considered a critical element of the AMOC.

Our findings are therefore qualitatively in accord with an important role of isopycnal stirring in the AMOC. A more quantitative measure of the significance of this role can be drawn directly from our observations. A time-scale for salinity homogeneisation by isopycnal stirring can be derived from the large-scale salinity variance over the eSPNA on a representative isopycnal (e.g., a standard deviation of $\mathrm{std}(S_A) = 0.3 - 0.5$ g kg^{-1} at $\sigma_0 = 27.4$ kg m^{-3}, Fig. 1), and the regional-mean salinity variance dissipation due to isopycnal stirring ($\sim 5.3 \times 10^{-10}$ (g kg^{-1})^2 s^{-1}, Fig. 10a). The resulting time-scale ($\tau = \mathrm{std}(S_A)^2/\chi_S$) is in the range of 5-15 years. If such time-scale is representative of the upper ocean volume (depths of $h < 500$ m) over the surface area of the eSPNA between the BOCATS2 section and the Greenland-Iceland-Scotland ridge ($A \approx 3.8 \times 10^{12}$ m^2), isopycnal mixing could be responsible for $A\,h/\tau = 4 - 11$ Sv (1 Sv $= 10^6$ m^3 s^{-1}) of diahaline overturning.

These isopycnal transformations are smaller, but comparable to the mean diapycnal overturning circulation in the region (10-20 Sv, Lherminier et al. (2010); Lozier et al. (2019)), and consistent with the rates of formation of SPMW (García-Ibáñez et al., 2015; Stendardo et al., 2024). This simple analysis thus suggests that diahaline transformation by isopycnal stirring may be an important process in the formation of SPMW and, by extension, the AMOC. A drawback of this estimate is that our measurements have limited spatio-temporal coverage. A full assessment of the role of mixing in the AMOC's mean state and variability would require extensive microstructure observations across the subpolar gyre to resolve the range of spatio-temporal variability of mixing in the region.

Apart from the general dominance of isopycnal stirring, we observed substantial tracer-dependent regional variations in the relative importance of diapycnal and isopycnal processes across the eSPNA. These regional patterns appear to be primarily driven by the degree of co-variability between large-scale tracer and density distributions. In regions where the considered tracer is the primary driver of vertical density stratification, and thus highly correlated with density, diapycnal mixing plays a more prominent

role. For instance, thermal mixing is predominantly diapycnal in the thermally stratified WEB, and isopycnal in the EGC's halocline, where diapycnal mixing makes the largest contribution to salinity variance dissipation. In the Irminger Sea, where vertical density stratification is relatively weak, mixing is facilitated by the existence of thermohaline gradients on isopycnal surfaces, maintained by air-sea fluxes and the confluence of water masses from the northern (Arctic, Nordic Seas) and southern (subtropical) latitudes (Evans et al., 2023), leading to a dominant role of mesoscale turbulence. This dominance is more pronounced for salinity, which exhibits small diapycnal gradients.

The prevalence of diapycnal temperature mixing in the subtropically-influenced WEB aligns with the temperature variance budget of the subtropical thermocline at the North Atlantic Tracer Release Experiment (NATRE) site (25°N, 30°W) (Ferrari & Polzin, 2005). In contrast to temperature, salinity mixing in the WEB is governed by isopycnal stirring. It is possible that the substantial role of isopycnal stirring is specific to the WEB's location at the boundary between between the subtropical and subpolar gyres, where strong gradients exist along isopycnals, rather than representing a general characteristic of the subtropical thermocline. The WEB is the region of largest eddy kinetic energy in our sampling section (Fig. 1b), possibly contributing to the importance of eddy stirring there. However, strong isopycnal property gradients and evidence for isopycnal ventilation in the lower subtropical thermocline were also reported further south in the Azores region (Robbins et al., 2000).

The importance of isopycnal stirring in the SPMW layers of the Irminger Sea is consistent with thermal variance budget analyses in intermediate and deep waters of the Drake Passage and the Malvinas Confluence in the Southern Ocean (Naveira Garabato et al., 2016; Orúe-Echevarría et al., 2023). Our results endorse the hypothesis that properties in water masses outcropping at high latitudes are preferentially mixed along isopycnals (Naveira Garabato et al., 2017), while diapycnal mixing would be more important in the subtropical thermocline. It also emerges clearly that the relative importance of either process is strongly tracer-dependent, as well as region-dependent, yet current knowledge about this variability remains limited. A large-scale investigation of the relative importance of isopycnal stirring and diapycnal mixing would enhance our understanding of how heat and chemicals are redistributed within the ocean.

6 Conclusions

Using microstructure observations and a small-scale tracer variance conservation framework, our study has demonstrated that isopycnal stirring by mesoscale turbulence is the primary driver of heat and salt mixing in the upper eastern subpolar North Atlantic. Our findings are consistent with an important role of mixing in the formation of subpolar mode waters from central waters, which contributes to the AMOC, and emphasize the strong isopycnal nature of these transformations, a facet often overlooked in the conventional perception of the AMOC as a primarily diapycnal phenomenon.

Isopycnal stirring emerges as a particularly crucial mechanism for salinity mixing, with potential implications for the transport of salt to the subpolar gyre (Berglund et al., 2023), a factor directly impacting the AMOC by preconditioning the region for deep wintertime convection (Warren, 1983; Pradal & Gnanadesikan, 2014; Born et al., 2016). The assessment of mesoscale stirring's importance takes on new significance, especially in predicting how the AMOC might respond to increased freshwater input from melting ice (Ditlevsen, 2023). Despite the substantial challenge of quantifying isopycnal stirring from oceanographic observations (Abernathey et al., 2022), the application of the variance budget method considered here, along with the deployment of autonomous platforms like profiling floats equipped with turbulence sensors (Roemmich, 2019), offers a promising avenue for addressing this challenge and advancing our comprehension of the climatic role of ocean mixing.

Further, our extension of the small-scale variance budget method to tracers beyond temperature has unveiled the tracer-dependent nature of the relative significance of isopycnal stirring. This point is particularly relevant for tracers whose large-scale distribution is uncoupled from density, such as salinity in a temperature-stratified ocean and temperature in a salinity-stratified ocean. The decoupling from density becomes more significant for tracers with biological sources or sinks, underscoring the central role of isopycnal stirring in the ocean's biogeochemical cycles (Abernathey & Ferreira, 2015; Eden & Greatbatch, 2009; Bahl et al., 2019; Spingys et al., 2021). Investigating this phenomenon could be pursued by applying the variance budget method to data from an expanding fleet of biogeochemical Argo floats (Bittig, 2019; Roemmich, 2019), in conjunction with direct or indirect estimates of diapycnal mixing rates (Whalen et al., 2012).

7 Open Research

Hydographic and microstructure data collected during the BOCATS2 cruise are available at SEANOE (https://doi.org/10.17882/95607), associated resources can be found at UTM Data Centre (https://doi.org/10.20351/29SG20230608). The scripts used for microstructure data processing are available at ZENODO (Fernández Castro, 2023).

Acknowledgments

This research was supported by BOCATS2 (PID2019-104279GB-C21) project funded by MCIN/AEI/10.13039/501100011033 and by EuroGO-SHIP project (Horizon Europe #101094690). BFC is supported by NERC grants NE/W009528/1 and NE/Y002709/1. MF was funded by Juan de La Cierva Formación (FJC2019-038970-I, Ministerio de Ciencia e Innovación, Spanish Government). DFR was supported by a FPU predoctoral fellowship (FPU2021/04749) from the Spanish Ministerio de Universidades. We thank the crew members of the R/V Sarmiento de Gamboa and the technicians for their work at sea.

References

Abernathey, R., & Ferreira, D. (2015). Southern Ocean isopycnal mixing and ventilation changes driven by winds. *Geophysical Research Letters*, *42*(23). doi: 10.1002/2015GL066238

Abernathey, R., Gnanadesikan, A., Pradal, M.-A., & Sundermeyer, M. A. (2022). Isopycnal mixing. In *Ocean Mixing* (pp. 215–256). Elsevier. doi: 10.1016/B978-0-12-821512-8.00016-5

Bahl, A., Gnanadesikan, A., & Pradal, M. (2019). Variations in Ocean Deoxygenation Across Earth System Models: Isolating the Role of Parameterized Lateral Mixing. *Global Biogeochemical Cycles*, *33*(6), 703–724. doi: 10.1029/2018GB006121

Bebieva, Y., & Lozier, M. S. (2023). Fresh Water and Atmospheric Cooling Control on Density-Compensated Overturning in the Labrador Sea. *Journal of Physical Oceanography*, *53*(11), 2575–2589. doi: 10.1175/JPO-D-22-0238.1

Berglund, S., Döös, K., Groeskamp, S., & McDougall, T. (2023, July). North Atlantic Ocean Circulation and Related Exchange of Heat and Salt Between Water Masses. *Geophysical Research Letters*, *50*(13), e2022GL100989. doi: 10.1029/2022GL100989

Bittig, H. C. (2019). A BGC-Argo Guide: Planning, Deployment, Data Handling and Usage. *Frontiers in Marine Science*, *6*, 502. doi: 10.3389/fmars.2019.00502

Born, A., Stocker, T. F., & Sandø, A. B. (2016). Transport of salt and freshwater in the Atlantic Subpolar Gyre. *Ocean Dynamics*, *66*(9), 1051–1064. doi: 10.1007/s10236-016-0970-y

Boyer, T. P., Garcia, H. E., Locarnini, R. A., Zweng, M. M., Mishonov, A. V., Rea-

gan, J. R., ... Smolyar, I. V. (2018). *World Ocean Atlas 2018.* Retrieved from `https://www.ncei.noaa.gov/archive/accession/NCEI-WOA18`

Brambilla, E., & Talley, L. D. (2008). Subpolar Mode Water in the northeastern Atlantic: 1. Averaged properties and mean circulation. *Journal of Geophysical Research*, *113*, C04025. doi: 10.1029/2006JC004062

Brüggemann, N., & Katsman, C. A. (2019). Dynamics of Downwelling in an Eddying Marginal Sea: Contrasting the Eulerian and the Isopycnal Perspective. *Journal of Physical Oceanography*, *49*(11), 3017–3035. doi: 10.1175/JPO-D-19-0090.1

Daniault, N., Mercier, H., Lherminier, P., Sarafanov, A., Falina, A., Zunino, P., ... Gladyshev, S. (2016). The northern North Atlantic Ocean mean circulation in the early 21st century. *Progress in Oceanography*, *146*, 142–158. doi: 10.1016/j.pocean.2016.06.007

Davis, R. E. (1994). Diapycnal Mixing in the Ocean: The Osborn–Cox Model. *Journal of Physical Oceanography*, *24*(12), 2560 – 2576. doi: 10.1175/1520-0485(1994)024⟨2560:DMITOT⟩2.0.CO;2

De Jong, M. F., Van Aken, H. M., Våge, K., & Pickart, R. S. (2012). Convective mixing in the central Irminger Sea: 2002–2010. *Deep Sea Research Part I: Oceanographic Research Papers*, *63*, 36–51. doi: 10.1016/j.dsr.2012.01.003

de Lavergne, C., Vic, C., Madec, G., Roquet, F., Waterhouse, A. F., Whalen, C. B., ... Hibiya, T. (2020). A Parameterization of Local and Remote Tidal Mixing. *Journal of Advances in Modeling Earth Systems*, *12*(5), e2020MS002065. doi: 10.1029/2020MS002065

Desbruyères, D., Chafik, L., & Maze, G. (2021, February). A shift in the ocean circulation has warmed the subpolar North Atlantic Ocean since 2016. *Communications Earth & Environment*, *2*(1), 48. doi: 10.1038/s43247-021-00120-y

Ditlevsen, P. (2023). Warning of a forthcoming collapse of the Atlantic meridional overturning circulation. *Nature Communications*, *14*, 4254. doi: 10.1038/s41467-023-39810-w

Eden, C., & Greatbatch, R. J. (2009). A diagnosis of isopycnal mixing by mesoscale eddies. *Ocean Modelling*, *27*(1-2), 98–106. doi: 10.1016/j.ocemod.2008.12.002

Evans, D. G., Holliday, N. P., Bacon, S., & Le Bras, I. (2023). Mixing and air–sea buoyancy fluxes set the time-mean overturning circulation in the subpolar North Atlantic and Nordic Seas. *Ocean Science*, *19*(3), 745–768. doi: 10.5194/os-19-745-2023

Fernández Castro, B. (2023). *[Software] Microstructure processing code (MSS) - BOCATS2 cruise.* Zenodo. doi: 10.5281/zenodo.10267840

Fernández Castro, B., Peña, M., Nogueira, E., Gilcoto, M., Broullón, E., Comesaña, A., ... Mouriño-Carballido, B. (2022). Intense upper ocean mixing due to large aggregations of spawning fish. *Nature Geoscience*, *15*(4), 287–292. doi: 10.1038/s41561-022-00916-3

Ferrari, R., & Polzin, K. L. (2005). Finescale Structure of the T–S Relation in the Eastern North Atlantic. *Journal of Physical Oceanography*, *35*(8), 1437–1454. doi: 10.1175/JPO2763.1

Ferron, B., Kokoszka, F., Mercier, H., & Lherminier, P. (2014). Dissipation Rate Estimates from Microstructure and Finescale Internal Wave Observations along the A25 Greenland–Portugal OVIDE Line. *Journal of Atmospheric and Oceanic Technology*, *31*(11), 2530–2543. doi: 10.1175/JTECH-D-14-00036.1

García-Ibáñez, M. I., Pardo, P. C., Carracedo, L. I., Mercier, H., Lherminier, P., Ríos, A. F., & Pérez, F. F. (2015). Structure, transports and transformations of the water masses in the Atlantic Subpolar Gyre. *Progress in Oceanography*, *135*, 18–36. doi: 10.1016/j.pocean.2015.03.009

Garrett, C. (2001). Stirring and Mixing: What are the Rate-Controlling Processes? *Stirring to mixing in a stratified ocean. Proceedings Hawaiian Winter Workshop [12th] Held in the University of Hawaii at Manoa.*

Groeskamp, S., LaCasce, J. H., McDougall, T. J., & Rogé, M. (2020). Full-Depth Global Estimates of Ocean Mesoscale Eddy Mixing From Observations and Theory. *Geophysical Research Letters*, *47*(18), e2020GL089425. doi: 10.1029/2020GL089425

Holliday, N. P., Bersch, M., Berx, B., Chafik, L., Cunningham, S., Florindo-López, C., ... Yashayaev, I. (2020, January). Ocean circulation causes the largest freshening event for 120 years in eastern subpolar North Atlantic. *Nature Communications*, *11*(1), 585. doi: 10.1038/s41467-020-14474-y

Ijichi, T., St. Laurent, L., Polzin, K. L., & Toole, J. M. (2020). How Variable Is Mixing Efficiency in the Abyss? *Geophysical Research Letters*, *47*(7), e2019GL086813. doi: 10.1029/2019GL086813

Joyce, T. M. (1977). A Note on the Lateral Mixing of Water Masses. *Journal of Physical Oceanography*, *7*(4), 626 – 629. doi: 10.1175/1520-0485(1977)007⟨0626:ANOTLM⟩2.0.CO;2

Jurado, E., Dijkstra, H. A., & van der Woerd, H. J. (2012). Microstructure observations during the spring 2011 STRATIPHYT-II cruise in the northeast Atlantic. *Ocean Science*, *8*(6), 945–957. doi: 10.5194/os-8-945-2012

Jurado, E., van der Woerd, H. J., & Dijkstra, H. A. (2012). Microstructure measurements along a quasi-meridional transect in the northeastern Atlantic Ocean. *Journal of Geophysical Research: Oceans*, *117*(C4). doi: 10.1029/2011JC007137

Kunze, E., Lien, R.-C., Whalen, C. B., Girton, J. B., Ma, B., & Buijsman, M. C. (2023, December). Seasonal Variability of Near-Inertial/Semidiurnal Fluctuations and Turbulence in the Subarctic North Atlantic. *Journal of Physical Oceanography*, *53*(12), 2717–2735. doi: 10.1175/JPO-D-22-0231.1

Lauderdale, J. M., Bacon, S., Naveira Garabato, A. C., & Holliday, N. P. (2008). Intensified turbulent mixing in the boundary current system of southern Greenland. *Geophysical Research Letters*, *35*(4), L04611. doi: 10.1029/2007GL032785

Lazier, J., Hendry, R., Clarke, A., Yashayaev, I., & Rhines, P. (2002). Convection and restratification in the Labrador Sea,. *Deep Sea Research Part I: Oceanographic Research Papers*, *49*, 1819–1835.

Le Bras, I. A., Straneo, F., Holte, J., De Jong, M. F., & Holliday, N. P. (2020). Rapid Export of Waters Formed by Convection Near the Irminger Sea's Western Boundary. *Geophysical Research Letters*, *47*(3), e2019GL085989. doi: 10.1029/2019GL085989

Lee, M.-M., Marshall, D. P., & Williams, R. G. (1997). On the eddy transfer of tracers: Advective or diffusive? *Journal of Marine Research*, *55*(3), 483–505. doi: 10.1357/0022240973224346

Lherminier, P., Mercier, H., Huck, T., Gourcuff, C., Perez, F. F., Morin, P., ... Falina, A. (2010). The Atlantic Meridional Overturning Circulation and the subpolar gyre observed at the A25-OVIDE section in June 2002 and 2004. *Deep-Sea Research I*, *57*(11), 1374–1391. doi: 10.1016/j.dsr.2010.07.009

Lherminier, P., Velo, A., Perez, F. F., Le Bihan, C., Hamon, M., Le Bot, P., ... Lasa Gonzales, A. (2023). *BOCATS2 2023 Cruise data along the A25-OVIDE section.* SEANOE. Retrieved from `https://www.seanoe.org/data/00844/95607/` doi: 10.17882/95607

Lozier, M. S., Li, F., Bacon, S., Bahr, F., Bower, A. S., Cunningham, S. A., ... Zhao, J. (2019). A sea change in our view of overturning in the subpolar North Atlantic. *Science*, *363*(6426), 516–521. doi: 10.1126/science.aau6592

Mackay, N., Wilson, C., Holliday, N. P., & Zika, J. D. (2020). The Observation-Based Application of a Regional Thermohaline Inverse Method to Diagnose the Formation and Transformation of Water Masses North of the OSNAP Array from 2013 to 2015. *Journal of Physical Oceanography*, *50*(6), 1533–1555. doi: 10.1175/JPO-D-19-0188.1

Marsh, R. (2000). Recent Variability of the North Atlantic Thermohaline Circulation Inferred from Surface Heat and Freshwater Fluxes. *Journal of Climate*, *13*(18), 3239–3260. doi: 10.1175/1520-0442(2000)013⟨3239:RVOTNA⟩2.0.CO;2

McCartney, M. S., & Talley, L. D. (1982). The Subpolar Mode Water of the North Atlantic Ocean. *Journal of Physical Oceanography*, *12*(11), 1169–1188. (ISBN: 0022-3670) doi: 10.1175/1520-0485(1982)012⟨1169:TSMWOT⟩2.0.CO;2

Naveira Garabato, A. C., MacGilchrist, G. A., Brown, P. J., Evans, D. G., Meijers, A. J. S., & Zika, J. D. (2017). High-latitude ocean ventilation and its role in Earth's climate transitions. *Philosophical Transactions of the Royal Society A: Mathematical, Physical and Engineering Sciences*, *375*(2102), 20160324. doi: 10.1098/rsta.2016.0324

Naveira Garabato, A. C., Polzin, K. L., Ferrari, R., Zika, J. D., & Forryan, A. (2016). A Microscale View of Mixing and Overturning across the Antarctic Circumpolar Current. *Journal of Physical Oceanography*, *46*(1), 233–254. doi: 10.1175/JPO-D-15-0025.1

Oakey, N. S. (1982). Determination of the Rate of Dissipation of Turbulent Energy from Simultaneous Temperature and Velocity Shear Microstructure Measurements. *J. Phys. Oceanogr*, *12*(3), 256–271.

Orúe-Echevarría, D., Polzin, K. L., Naveira Garabato, A. C., Forryan, A., & Pelegrí, J. L. (2023). Mixing and Overturning Across the Brazil-Malvinas Confluence. *Journal of Geophysical Research: Oceans*, *128*(5), e2022JC018730. doi: 10.1029/2022JC018730

Osborn, T. R. (1980). Estimates of the local rate of vertical diffusion from dissipation measurements. *Journal of Physical Oceanography*, *10*, 83–89. doi: 10.1175/1520-0485(1980)010⟨0083:EOTLRO⟩2.0.CO;2

Osborn, T. R., & Cox, C. S. (1972, January). Oceanic fine structure. *Geophysical Fluid Dynamics*, *3*(1), 321–345. doi: 10.1080/03091927208236085

Petit, T., Lozier, M. S., Josey, S. A., & Cunningham, S. A. (2020). Atlantic Deep Water Formation Occurs Primarily in the Iceland Basin and Irminger Sea by Local Buoyancy Forcing. *Geophysical Research Letters*, *47*(22), e2020GL091028. doi: 10.1029/2020GL091028

Piccolroaz, S., Fernández-Castro, B., Toffolon, M., & Dijkstra, H. A. (2021). A multi-site, year-round turbulence microstructure atlas for the deep perialpine Lake Garda. *Scientific Data*, *8*(1), 188. doi: 10.1038/s41597-021-00965-0

Pickart, R. S., Straneo, F., & Moore, G. W. K. (2003). Is Labrador Sea Water formed in the Irminger basin? *Deep-Sea Research I*, *50*(1), 23–52. doi: 10.1016/S0967-0637(02)00134-6

Pradal, M.-A., & Gnanadesikan, A. (2014). How does the Redi parameter for mesoscale mixing impact global climate in an Earth System Model? *Journal of Advances in Modeling Earth Systems*, *6*, 586–601. doi: 10.1002/2013MS000273

Prandke, H., & Stips, A. (1998). Test measurements with an operational microstructure-turbulence profiler: Detection limit of dissipation rates. *Aquatic Science*, *60*(3), 191–209. (ISBN: 1015-1621) doi: 10.1007/s000270050036

Pérez, F. F., Mercier, H., Vázquez-Rodríguez, M., Lherminier, P., Velo, A., Pardo, P. C., ... Ríos, A. F. (2013). Atlantic Ocean CO2 uptake reduced by weakening of the meridional overturning circulation. *Nature Geoscience*, *6*(2), 146–152. doi: 10.1038/ngeo1680

Robbins, P. E., Price, J. F., Owens, W. B., & Jenkins, W. J. (2000). The Importance of Lateral Diffusion for the Ventilation of the Lower Thermocline in the Subtropical North Atlantic. *Journal of Physical Oceanography*, *30*, 67–89.

Roemmich, D. (2019). On the Future of Argo: A Global, Full-Depth, Multi-Disciplinary Array. *Frontiers in Marine Science*, *6*, 439. doi: 10.3389/fmars.2019.00439

Spingys, C. P., Williams, R. G., Tuerena, R. E., Naveira Garabato, A., Vic, C., Forryan, A., & Sharples, J. (2021). Observations of Nutrient Supply by Mesoscale Eddy Stirring and Small-Scale Turbulence in the Oligotrophic North Atlantic. *Global Biogeochemical Cycles*, *35*(12), e2021GB007200. doi: 10.1029/2021GB007200

Stendardo, I., Buongiorno Nardelli, B., Durante, S., Iudicone, D., & Kieke, D. (2024). Interannual Variability of Subpolar Mode Water in the Subpolar North Atlantic. *Journal of Geophysical Research: Oceans*, *129*(3), e2023JC019937. doi: 10.1029/2023JC019937

St Laurent, o., & Schmitt, R. W. (1999). The Contribution of Salt Fingers to Vertical Mixing in the North Atlantic Tracer Release Experiment. *Journal of Physical Oceanography*, *29*(7), 1404–1424. doi: 10.1175/1520-0485(1999)029⟨1404:TCOSFT⟩2.0.CO;2

Straneo, F. (2006). On the Connection between Dense Water Formation, Overturning, and Poleward Heat Transport in a Convective Basin*. *Journal of Physical Oceanography*, *36*(9), 1822–1840. doi: 10.1175/JPO2932.1

Tooth, O. J., Johnson, H. L., Wilson, C., & Evans, D. G. (2023). Seasonal overturning variability in the eastern North Atlantic subpolar gyre: a Lagrangian perspective. *Ocean Science*, *19*(3), 769–791. doi: 10.5194/os-19-769-2023

Warren, B. A. (1983). Why is no deep water formed in the North Pacific? *Journal of Marine Research*, *41*, 327–347.

Waterhouse, A. F., MacKinnon, J. A., Nash, J. D., Alford, M. H., Kunze, E., Simmons, H. L., ... Lee, C. M. (2014). Global Patterns of Diapycnal Mixing from Measurements of the Turbulent Dissipation Rate. *Journal of Physical Oceanography*, *44*(7), 1854–1872. doi: 10.1175/JPO-D-13-0104.1

Whalen, C. B., Talley, L. D., & MacKinnon, J. A. (2012). Spatial and temporal variability of global ocean mixing inferred from Argo profiles. *Geophysical Research Letters*, *39*(18). doi: 10.1029/2012GL053196

Xu, X., Rhines, P. B., & Chassignet, E. P. (2018). On Mapping the Diapycnal Water Mass Transformation of the Upper North Atlantic Ocean. *Journal of Physical Oceanography*, *48*, 2233–2258. doi: 10.1175/JPO-D-17-0223.1

Yeager, S., Castruccio, F., Chang, P., Danabasoglu, G., Maroon, E., Small, J., ... Zhang, S. (2021, October). An outsized role for the Labrador Sea in the multidecadal variability of the Atlantic overturning circulation. *Science Advances*, *7*(41), eabh3592. (Publisher: American Association for the Advancement of Science) doi: 10.1126/sciadv.abh3592

Zou, S., Lozier, M. S., Li, F., Abernathey, R., & Jackson, L. (2020). Density-compensated overturning in the Labrador Sea. *Nature Geoscience*, *13*(2), 121–126. doi: 10.1038/s41561-019-0517-1

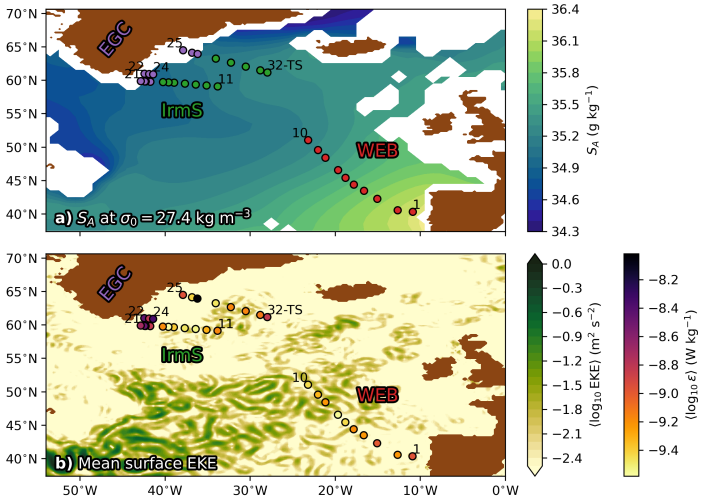

Figure 1. Maps of the BOCATS2 cruise microstructure stations. Dots indicate the station positions and are color-coded by (a) sampling region (Red: Western European Basin, WEB, stations 1-10; Green: Irminger Sea, IrmS, stations 11-17, 28-32; Purple: East Greenland Current, EGC, stations 18-27), and (b) mean value of ε below 50 m depth. Station numbers for the beginning and end of each sub-transect are shown, together with labels for the three analysis regions. The background contours represent: (a) climatological absolute salinity S_A distribution at the $\sigma_0 = 27.4$ kg m^{-3} isopycnal based on the World Ocean Atlas 2018 (Boyer et al., 2018), (b) mean satellite-derived eddy kinetic energy over the cruise duration (dataset dataset-duacs-nrt-global-merged-allsat-phy-l4 from https://marine.copernicus.eu). The basin-scale contrast of salinity on an isopycnal (a) illustrates the large density-compensated thermohaline gradients characterizing in this region, which provide necessary conditions for isopycnal stirring to have a relevant contribution to mixing.

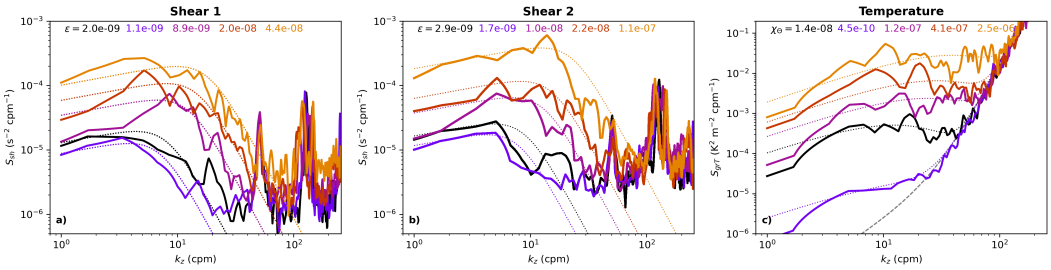

Figure 2. Microstructure spectra. Randomly selected vertical wavenumber (k_z) spectra, from shear sensor 1 (a), shear sensor 2 (b), and thermistor (c), respectively, and for ε values in the range 10^{-10} – 10^{-6} W kg^{-1}. Dotted lines show the corresponding empirical spectra obtained through spectral integration (shear) or fitting to the Kraichnan spectrum (temperature). The thermistor's theoretical noise curve is shown as a gray dashed line. The derived ε (W kg^{-1}) and χ_Θ (K^2 s^{-1}) values are reported.

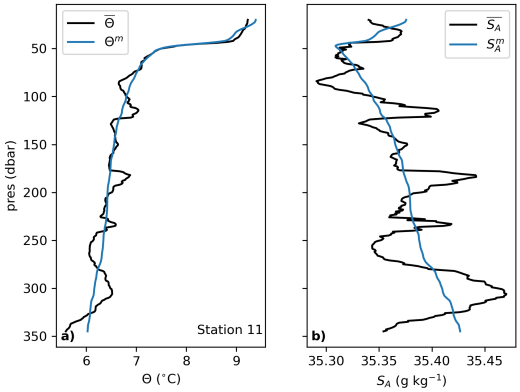

Figure 3. Obtaining the background profiles. Example profile (station 11, profile 2), showing results from the polynomial fit (Eq. 7) used to obtain the background (or large-scale mean flow, in the conventional terminology) profiles of conservative temperature (Θ^m, a) and absolute salinity (S_A, b) from the CTD-observed profiles ($\overline{\Theta}$ and $\overline{S}_A$, respectively). These profiles exhibit pronounced density-compensated thermohaline fine-scale structures resulting from eddy stirring. Such structures are effectively removed by the polynomial fit of the corresponding tracer against potential density.

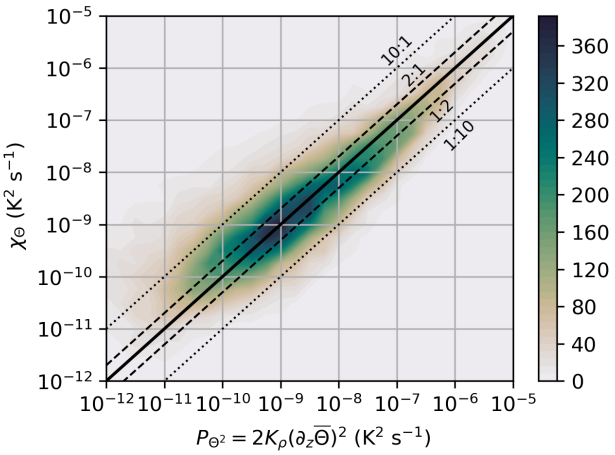

Figure 4. Small-scale variance production and dissipation. Two-dimensional histogram of thermal variance dissipation rate (χ_Θ) and small-scale thermal variance production due to the action of microscale turbulent motions on the fine-scale resolved conservative temperature profile (P_{Θ^2}), which includes the contributions from the mean flow and the mesoscale eddy components, in the context of the triple decomposition framework. The solid line indicates a one-to-one correspondence, and the dashed and dotted lines delimit agreement within a factor of 2 and 10, respectively.

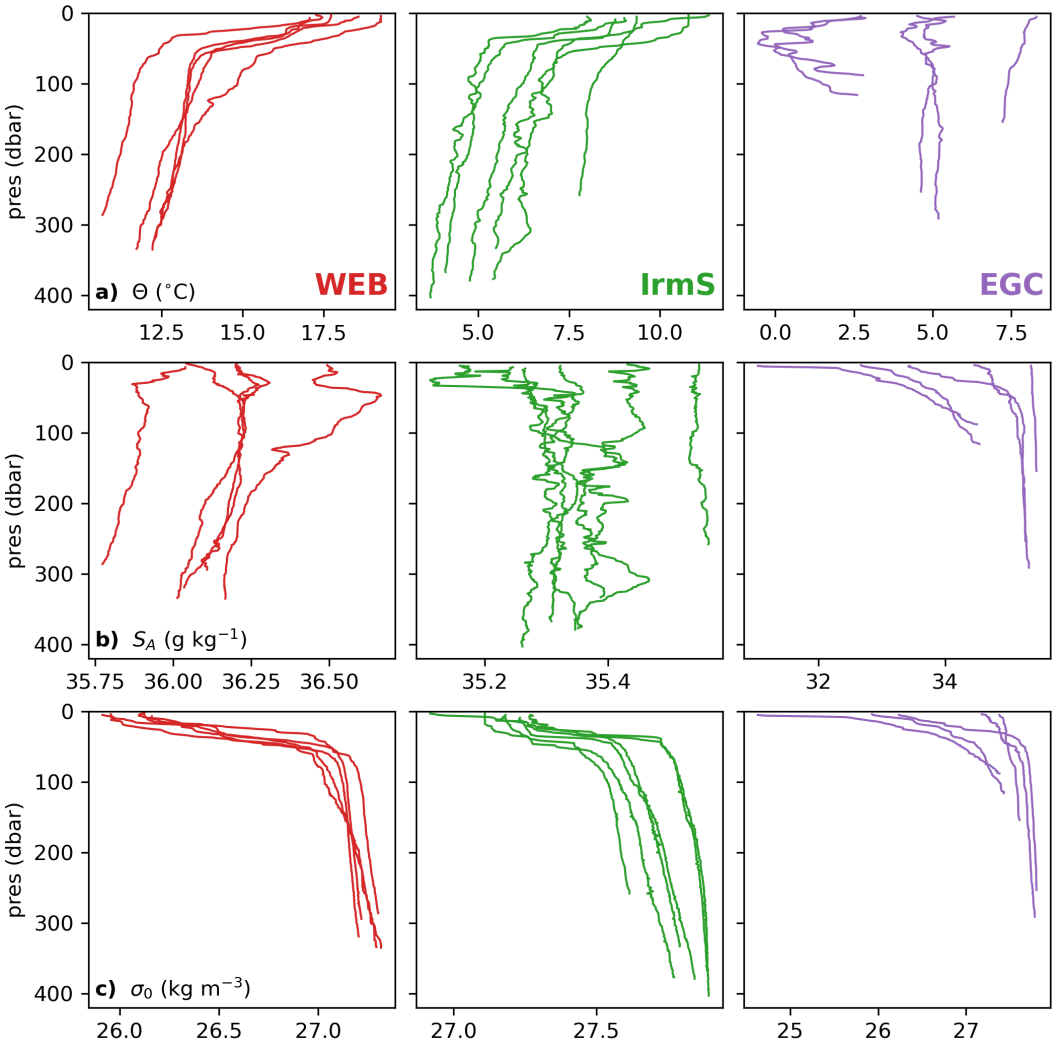

Figure 5. Hydrographic profiles. Example profiles of (a) conservative temperature (Θ), (b) absolute salinity (S_A) and (c) potential density (σ_0) during the BOCATS2 cruise. One profile is shown for every other sampled station. Profiles are color coded by region (Red: Western European Basin, WEB; Green: Irminger Sea, IrmS; Purple: East Greenland Current, EGC).

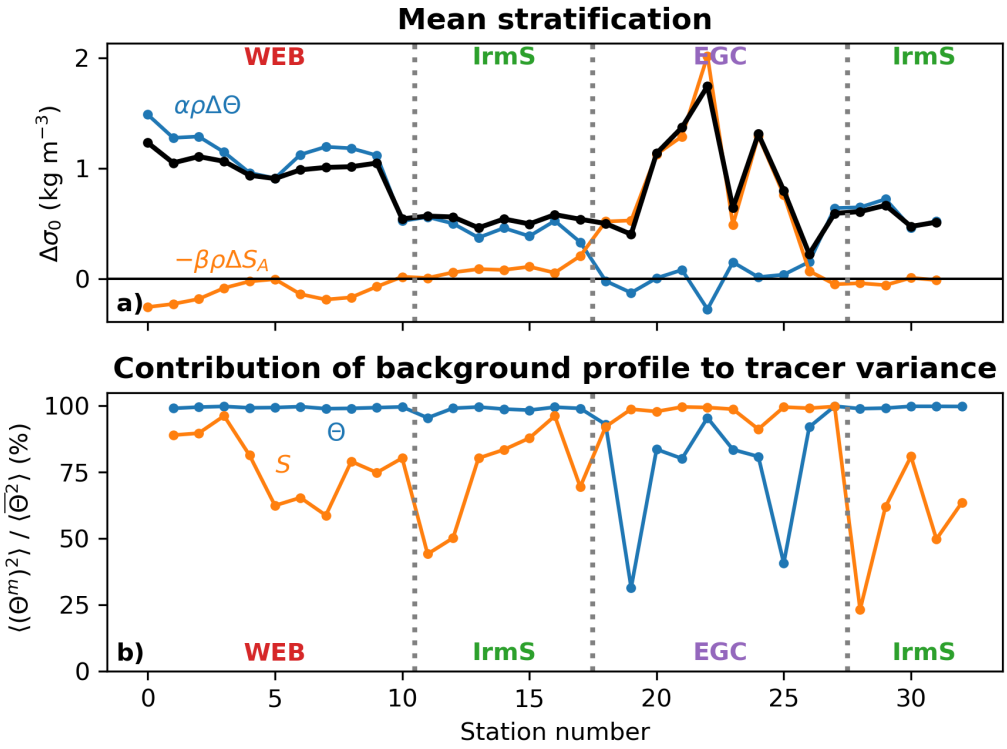

Figure 6. Stratification and vertical tracer variance. (a) Density difference between the top and the bottom of the MSS profile at each station ($\Delta\sigma_0$, black), alongside partial contributions from temperature ($\alpha\rho\Delta\Theta$) and salinity (-$\beta\rho\Delta S_A$). (b) Ratio between the variance of the background (or "large-scale mean") component of Θ (blue) (and S_A, orange), $\langle(\Theta^m)^2\rangle$, to the total variance of the measured Θ (and S_A) profiles, $\langle(\overline{\Theta})^2\rangle$.

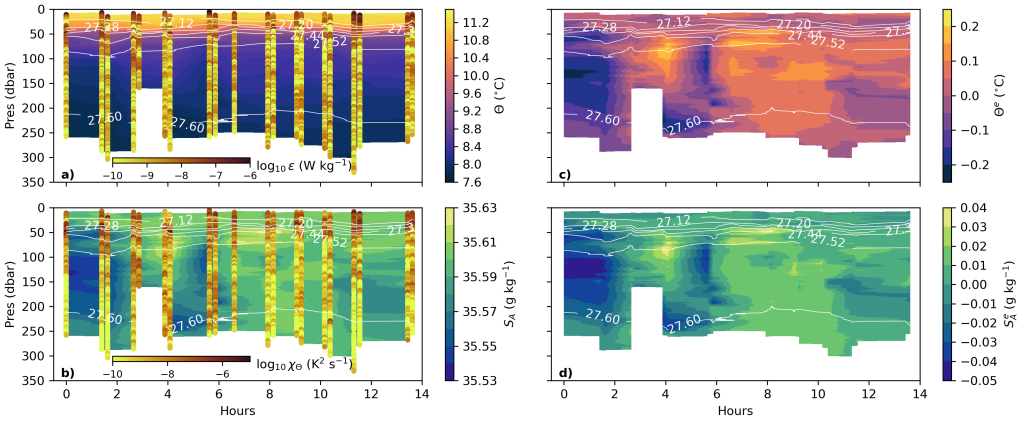

Figure 7. Hydrographic profiles at time-series station 32 over the Reykjanes Ridge. (a, b) 14-hours time-series of conservative temperature (Θ) and practical salinity (S_A) vertical profiles, with potential density contours (white) overlaid. Profiles of the dissipation rates of turbulent kinetic energy (ε) and thermal variance (χ_Θ) are shown as colored dots. (c, d) conservative temperature and salinity mesoscale anomaly profiles (Θ^e, S_A^e, respectively), computed with respect to the time-mean profiles in σ_0 coordinates.

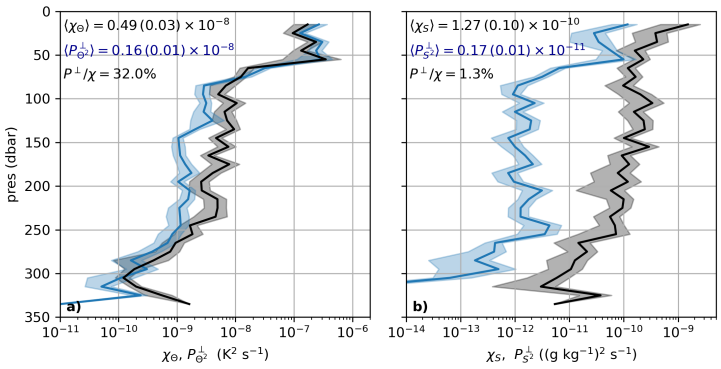

Figure 8. Mixing rates at time-series station 32 over the Reykjanes Ridge. Time-mean profiles of the dissipation rates of thermal (a) and salinity (b) variance (χ_Θ, χ_S, black), along with small-scale variance production by microscale turbulence ($P^\perp_{\Theta^2}$, $P^\perp_{S^2}$, blue). Error bars (shading) represent ±2 standard errors. Mean values of χ and $P^\perp$ below 100 m depth, and their ratio, are reported.

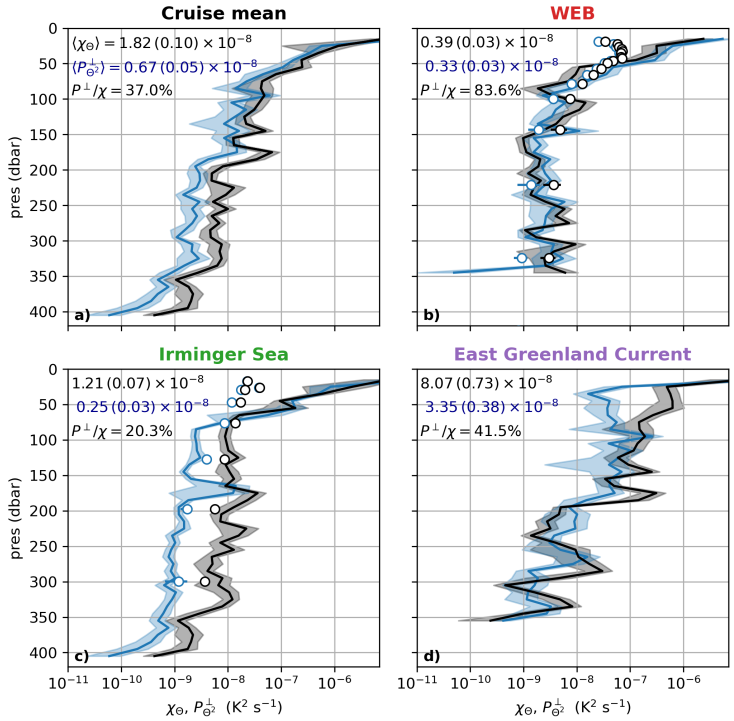

Figure 9. Cruise-mean thermal mixing rate profiles. Mean profiles (solid lines) of the dissipation rates of thermal variance (χ_Θ), along with small-scale variance production by microscale turbulence ($P^\perp_{\Theta^2}$, blue) for the entire cruise (a), and for the different analysis regions: Western European Basin, WEB (b); Irminger Sea, IrmS (c); East Greenland Current, EGC (d). Error bars (shading) represent ±2 standard errors. Mean values of χ and $P^\perp$ below 100 m depth, and their ratio, are reported. Dots show estimates of $P^\perp_{\Theta^2}$ and χ_Θ (computed as $\chi_\Theta = P^\perp_{\Theta^2} + P^{||}_{\Theta^2}$) from climatological temperature fields (Boyer et al., 2018) and global diffusivity databases (Groeskamp et al., 2020; de Lavergne et al., 2020).

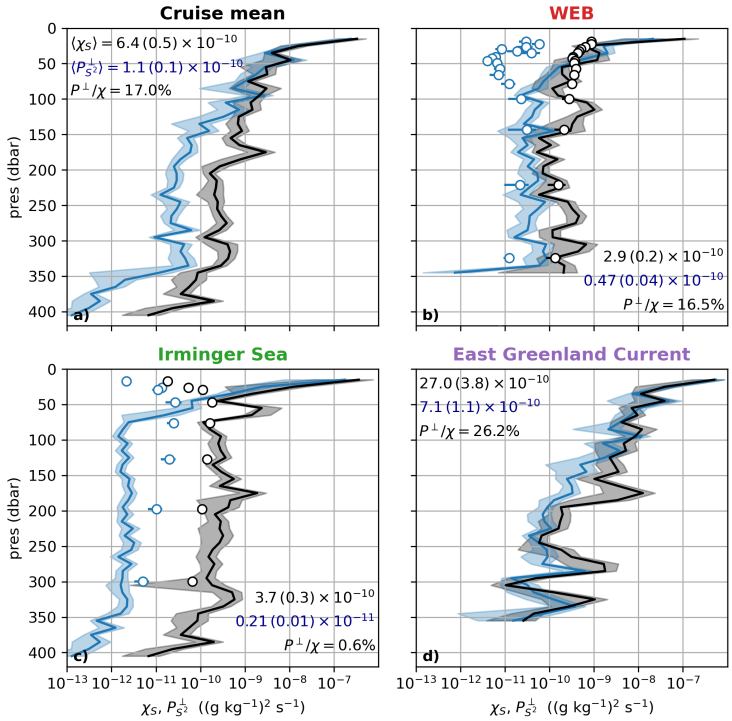

Figure 10. Cruise-mean haline mixing rate profiles. Mean profiles (solid lines) of the dissipation rates of salinity variance (χ_S, black), along with small-scale variance production by microscale turbulence ($P^{\perp}_{S^2}$, blue) for the entire cruise (a, f), and for the different analysis regions: Western European Basin, WEB (b); Irminger Sea, IrmS (c); East Greenland Current, EGC (d). Error bars (shading) represent ±2 standard errors. Mean values of χ and $P^{\perp}$ below 100 m depth, and their ratio, are reported. Dots show estimates of $P^{\perp}_{S^2}$ and χ_S (computed as $\chi_S = P^{\perp}_{S^2} + P^{||}_{S^2}$) from climatological salinity fields (Boyer et al., 2018) and global diffusivity databases (Groeskamp et al., 2020; de Lavergne et al., 2020).

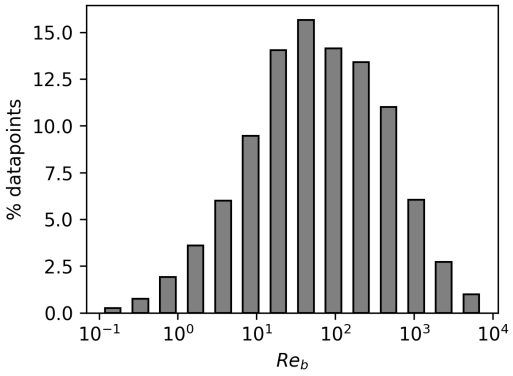

Figure 11. Turbulence regimes. Histogram of the buoyancy Reynolds number ($Re_b = \varepsilon/(\nu N^2)$, where ν is molecular viscosity). Includes all of the cruise data below 50 m depth.

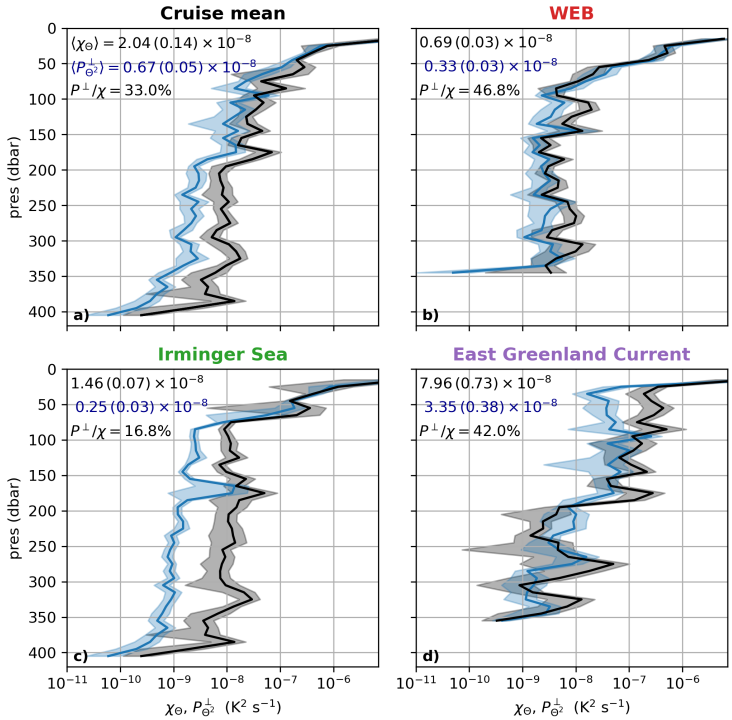

Figure 12. Same as Fig. 9 but χ_Θ estimated using the Osborn and Cox (1972) formula (Eq. 3) instead of direct measurements.

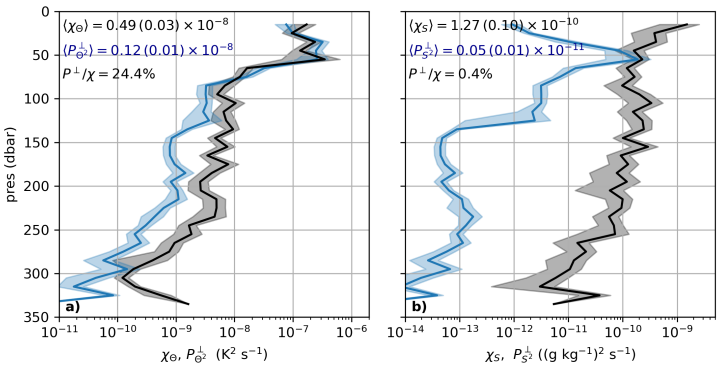

Figure 13. Same as Fig. 8 but with an alternative computation of $P^{\perp}_{\Theta^2}$ and $P^{\perp}_{S^2}$ based on the time-mean profiles of Θ and S_A as a function of σ_0.

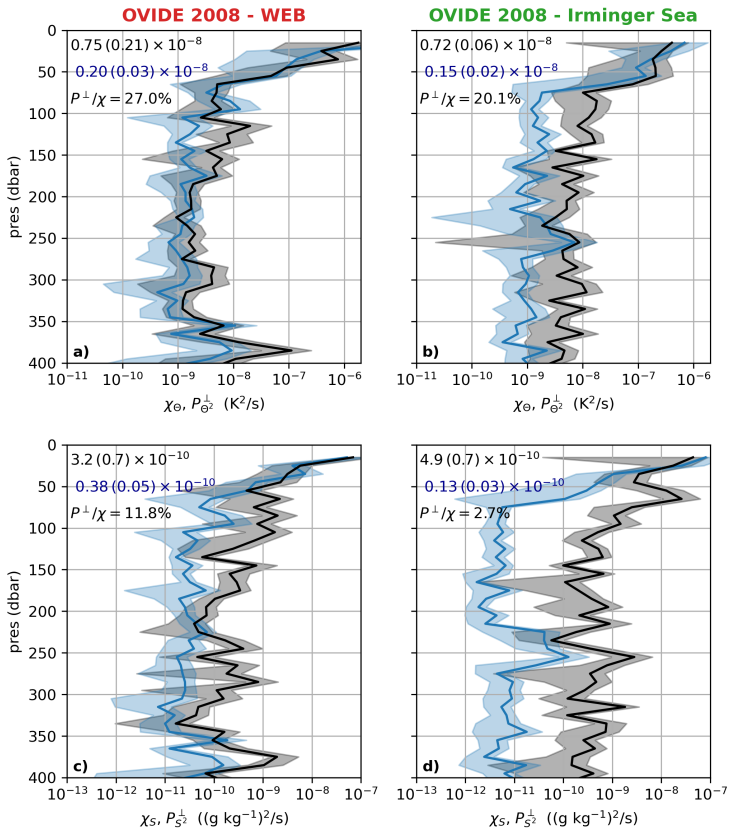

Figure 14. Mixing rates during the OVIDE cruise 2008. Mean profiles of the rates of thermal (a, b) and haline (c,d) variance dissipation (χ, black), along with small-scale variance production by microscale turbulence ($P^{\perp}$, blue) in the Western European Basin (a,c) and the Irminger Sea (b,d) during the OVIDE cruise 2008.